CERN- Data Handling Division
DD/77/15
A.P. Jeavons
D.W. Townsend
N.L. Ford
K. Kull *)
A. Manuel **)
O. Fischer **)
M. Peter **)
5 October 1977

A HIGH-RESOLUTION PROPORTIONAL CHAMBER POSITRON CAMERA AND ITS APPLICATIONS

Presented at the IEEE Nuclear Science Symposium,
San Francisco, 19-21 October, 1977

---

*) SB Division, CERN.

**) Departement de la Matière Condensée, Université de Genève, Switzerland.

DD/nf

A HIGH-RESOLUTION PROPORTIONAL CHAMBER POSITRON CAMERA AND ITS APPLICATIONS

A.P. Jeavons, D.W. Townsend, N.L. Ford and K. Kull
CERN, Geneva, Switzerland
and
A. Manuel, O. Fischer and M. Peter
Département de la Matière Condensée, Université de Genève, Switzerland

ABSTRACT

A positron camera consisting of two high density proportional chambers is described. It provides a spatial resolution of 2.4 mm FWHM, a maximum data rate of 3000 c.p.s. and a sensitivity of 25 c.p.s. per μCi. Results of its application to angular correlation studies of condensed matter and to phantom and in vivo medical imaging are presented. A Fourier deconvolution technique is described for obtaining three-dimensional medical images. It uses a generalized matrix inversion by singular value decomposition to modify the low frequency Fourier components.

Introduction

For many years the sodium iodide scintillation camera has been the standard instrument for imaging gamma rays.[1] However, despite much work, the best spatial resolution obtainable is about 7 mm FWHM, a considerable limitation. Another limitation arises when imaging gamma rays of high energy, e.g., 0.5 MeV. Since the photon capture cross-section by photo-electric effect falls rapidly with increasing energy, sodium iodide is more sensitive to lower energies, i.e. to spurious events resulting from Compton scattering of the initial high-energy photons. Energy selection can remove some of these events, but problems remain due to high pulse rates in the detector electronics.

Recently, it has been shown[2,3] that the addition of a high-density drift space to a proportional chamber affords an efficient gamma-ray detector with a spatial resolution of 1 mm FWHM. Energy selection is not possible, but by the very nature of the detector, sensitivity increases with increasing energy, the converse of the case of the scintillation camera. Furthermore, a relatively free choice exists for the material comprising the drift space converter: the use of lead, atomic number 82, is a natural choice for high-energy gamma rays.

Two chambers have been constructed specifically for detecting the two 0.511 MeV back-to-back coincident gamma rays resulting from positron annihilation. This positron camera has been applied to two well known problems: a) the determination of electron momentum distributions in condensed matter through the measurement of the angular correlation of the gamma-ray pairs,[4] and b) the measurement of the three-dimensional distributions of positron-active radioisotopes within the body.[5] This paper presents some details of the camera and the first results from these applications. A Fourier deconvolution technique is described for medical image reconstruction, using generalized matrix inversion by singular value decomposition to modify the low-frequency Fourier components.[6]

The Positron Camera

Chamber Construction and Operation

The principle of the high-density drift space is shown in Fig. 1. A solid block is perforated with a large number of holes close together. By making the block thick enough, a high probability will exist for converting photons to Compton or photo-electrons. With a correct choice of hole size and spacing, the electrons will have a high probability of escaping to a hole, but a low probability of propagating to a second hole. The application of an electric field to the block will drift the electrons resulting from gas ionization in the holes out of the block for subsequent detection by a proportional chamber. If the hole axis is parallel to the direction of the impinging photons, the two dimensions perpendicular to this direction may be resolved to an accuracy determined by the hole size. The electric field may be made to penetrate the holes by making the block of alternate metallic and insulating sheets, and connecting a resistor chain to the metallic sheets.

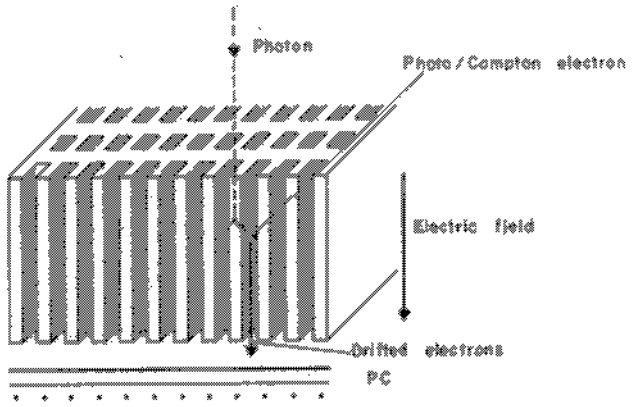

Fig. 1: The principle of the high-density drift space. Photons are captured in the solid bars and produce fast electrons which can escape to an adjacent hole. The free electrons, resulting from gas ionization in a hole, may be extracted by an electric field and detected by a proportional chamber.

Figure 2 shows one of the two chambers forming the camera. In each chamber there are two converters with an active area of 10 × 10 cm, one on each side of the wire planes. The two converters are offset so that the bars of the one are behind the holes of the other. Each converter is made of 75 lead-bismuth alloy plates 0.25 mm thick, interleaved with 0.1 mm thick glass-fibre epoxy resin sheets. The holes are 0.8 mm in diameter close-packed on an hexagonal pattern with a pitch of 1 mm. Proportional chamber construction follows normal techniques. Anode wires are of 20 μm gold-plated tungsten wire spaced at $\sqrt{3}$ mm (to fit behind the rows of holes) and cathode wires are 100 μm spaced at 1 mm. Anode to cathode interplane distance is 3 mm.

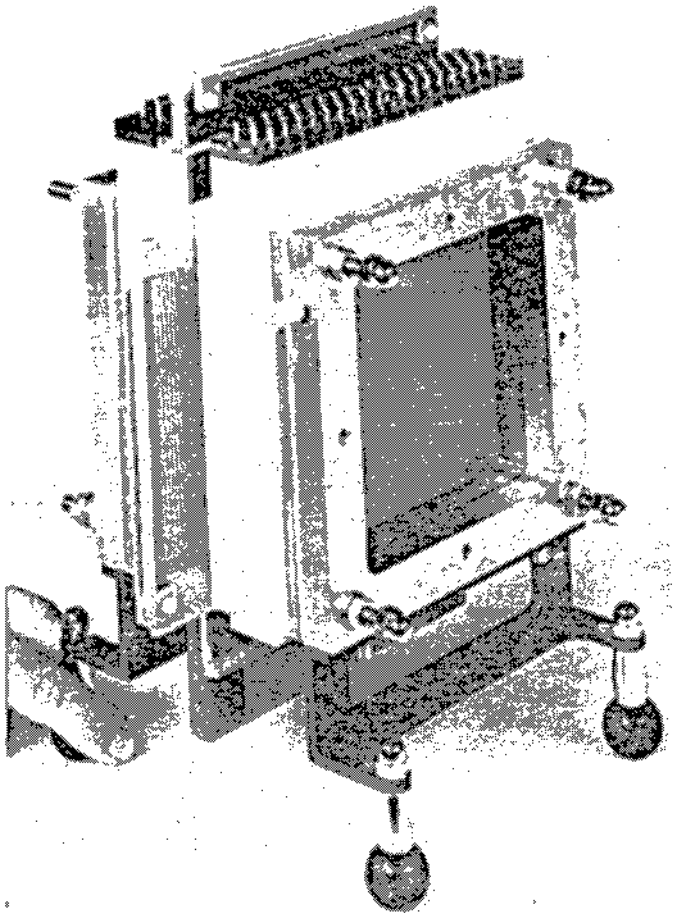

Fig. 2: A general view of one of the two chambers comprising the positron camera.

The chambers were operated with free-flow isobutane gas with 3.8 kV on the anode plane and 5 kV across the drift spaces. Readout was the digital centre-of-gravity technique:[7] signals on the cathode strips were digitized with CAMAC analogue-to-digital converters, and the centre of gravity of each event calculated by software with a PDP11/20 computer.

Chamber Performance

For 660 keV photons from ^{137}Cs, the detection efficiency of each chamber was measured to be 15% and the spatial resolution to be 1.2 mm FWHM: see Fig. 3. Operated in coincidence with positron annihilation radiation, the camera gave the time resolution shown in Fig. 4. The time jitter is due to the drift time of the electrons through the thickness of the converter. The cut-off at 500 nsec agrees with the known electron drift velocity, 5 cm/μsec, in isobutane, for two events separated by the full thickness, 25 mm, of a converter.

Angular Correlation Measurements

When a positron penetrates condensed matter, it thermalizes or loses its momentum before annihilating with an electron. It follows that the gamma-ray pair resulting from annihilation will then carry with it a knowledge of the momentum of the electron with which the positron annihilated. Thus positrons may be used as a probe for studying electron momentum distributions. A direct measure of such distributions may be made by mapping the angular differences of the two gamma-ray directions from 180^{o}. Since these angles are small, typically a few milliradians, a camera with a good spatial resolution is prerequisite. Traditionally, slit-collimated single sodium iodide counters are placed on either side of a specimen irradiated with positrons. The slits are moved to map out the angular distribution. Replacing these counters with the present camera provides two important advances: two-dimensional information, and a greatly increased data rate due to simultaneous collection over the full angular distribution. The results of a first measurement on a copper single crystal have already been reported.[8] Here a preliminary investigation of aluminium is reported.

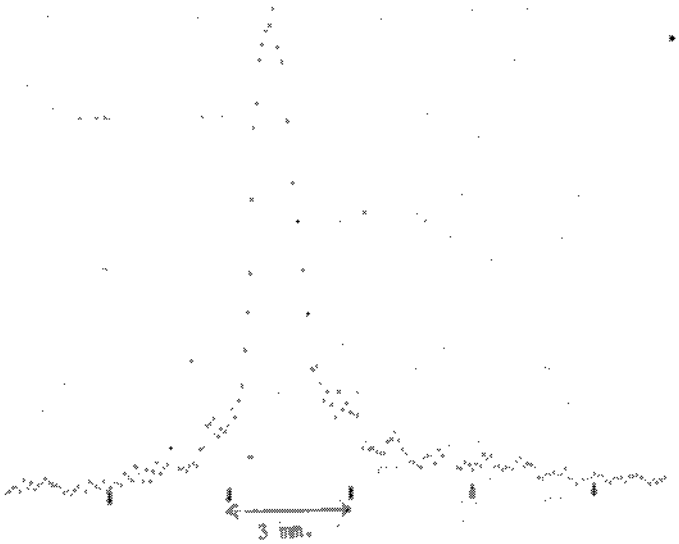

Fig. 3: The spatial resolution obtained from a chamber with 660 keV gamma rays collimated by a 0.5 mm slit. Tick marks are every 3 mm.

Fig. 4: The measured coincidence-time distribution of the camera. Full scale is 800 nsec; cut-off at 500 nsec.

Each chamber was placed at 4 m on either side of a single crystal of aluminium 10 × 3 × 1 mm, at room temperature, illuminated by a 50 mCi source of positrons ^{22}Na. The over-all angular resolution, due to the chambers and the crystal size, was estimated to be 0.7 × 0.5 mrad FWHM. $3 \cdot 10^{6}$ events were collected at a rate of 10 c.p.s. The result, after computer correction for the variation of camera detection efficiency with angle is shown in Fig. 5. It is a direct visualization of the well known spherical Fermi surface of aluminium.

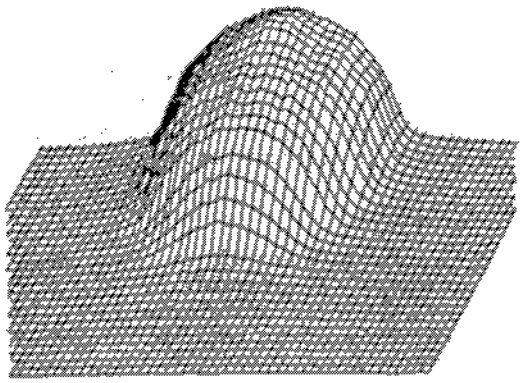

Fig. 5: The Fermi surface of aluminium as revealed by the measurement of the angular correlation of positron annihilation radiation. Horizontal axes: x angle against y angle. Vertical axis: number of events. Total number of events: $3 \cdot 10^6$. Grid size: 0.5 × 0.5 mrad. Number of events at the peak of the distribution: 5000. Distribution cut-off: 6.8 mrad.

The cut-off at 6.8 mrad marks the Fermi level of aluminium at 11.8 eV. Work now continues on a detailed study of the Fermi surface of copper.

Medical Positron Imaging

Imaging positron annihilation radiation offers a very significant advantage over conventional imaging. By recording, in coincidence, both of the back-to-back gamma rays, directional information is obtained as well as positional: no gamma-ray collimator is required, leading to a big increase in sensitivity and improvement of spatial resolution. In addition, tomographic reconstruction methods may be applied to provide three-dimensional images. Scintillation cameras, in various forms[9-13], are being applied to this problem. Spatial resolution ∿ 1 cm and sensitivity to Compton-scattered radiation seem to be the principal difficulties. Some work with proportional chambers has been reported[14,15]; spatial resolution is still poor and counting rates are low, 300 c.p.s., due to inadequate detection efficiencies.

Figure 6 shows the basic layout of the positron camera for medical imaging. By positioning various positron sources between the chambers on the object planes, and interposing scattering media, a systematic investigation of the application of the camera to medical imaging has been performed. The distance D between the chambers was typically 20 cm. Firstly, two important camera parameters, counting rate and spatial resolution are evaluated. Tomographic reconstruction methods are then explained and applied to phantom imaging. Finally, in vivo imaging of a mouse, injected with 5.7 μCi of ^{18}F, is presented.

Counting Rate

A fundamental limit to the counting rate of a positron camera arises from the occurrence of accidental coincidences. Suppose a point source of intensity I is placed midway between the detectors in Fig. 6. The solid angle acceptance of each detector is A, the detection efficiency E and the coincidence resolving time T. Since each positron annihilation produces two photons, the flux on each detector is 2IA and the

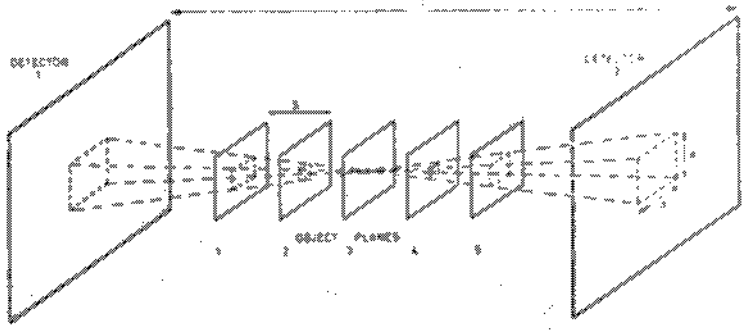

Fig. 6: The schematic layout of the positron camera.

detected event rate 2IAE. Neglecting Compton scattering, for every photon detected, its partner must hit the other detector so the coincidence signal rate is:

$$S = (2IAE) \cdot E \quad . \qquad (1)$$

The accidental coincidence rate, or noise N, is proportional to the event rate on each detector and to the resolving time:

$$N = (2IAE)^2 \cdot 2T \quad . \qquad (2)$$

Dividing (1) by (2), the signal-to-noise ratio is:

$$\frac{S}{N} = \frac{1}{4IAT} \quad . \qquad (3)$$

We see from (3), as is well known, that as I is increased, S/N degrades and may only be restored by decreasing T, since A is a constant for the camera. Thus for a particular resolving time there is a maximum source strength that may be accepted for a desired signal-to-noise ratio. Clearly, the smaller T the better. In this camera, T is quite long (maximum 500 nsec, see Fig. 4) and other designs have been proposed to shorten it. One scheme[16] puts the proportional chamber wires in the holes of the converter, whilst another[17] proposes wire planes between all the converter plates. However, Eq. (3) does not tell the full story: it just places a limit on source strength and this limit is smaller for a longer resolving time. This is, in fact, beneficial, by reducing the radioactive dose given to a patient. It does not follow that an adequate counting rate cannot be achieved. Substituting (3) into (1):

$$S = \frac{1}{2(S/N)} \cdot \frac{E^2}{T} \quad . \qquad (4)$$

Now we see that for fixed signal-to-noise ratio and resolving time, the counting rate may be improved by increasing the detection efficiency. E^2/T is a figure-of-merit for the camera, as far as counting rate is concerned. Clearly a small resolving time is desirable, but it is detection efficiency that is the more important factor. With the present camera, using one converter on each chamber, E was 7% and T was set to 400 nsec, giving an E^2/T figure-of-merit of $1.25 \cdot 10^4$ sec^{-1}. If S/N = 3 is assumed to be acceptable, then from (4), S = 2100 c.p.s. Acceptable images would be expected up to a counting rate of about 2000 c.p.s. This was investigated experimentally. A small bottle containing a ^{18}F isotope was imaged three times as the ^{18}F decayed. The result is shown in Figs. 7a, b, c. There is little difference between the images at 300 and 1000 c.p.s., but by 2800 c.p.s., image quality has obviously deteriorated. As it is quite reasonable to envisage raising E to about 20% in a future camera, E^2/T will increase by an order of magnitude, and the maximum

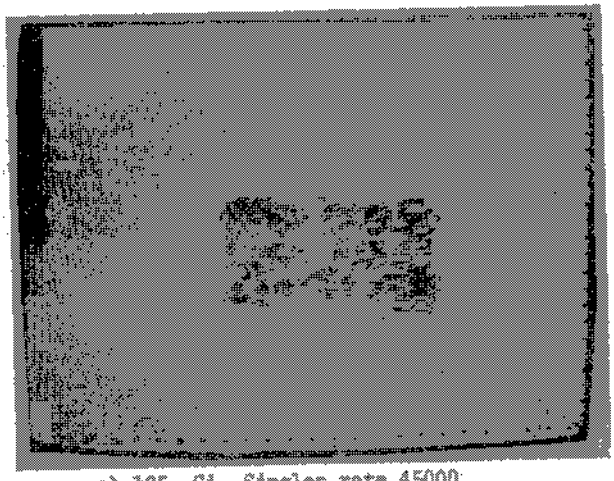

a) 125 μCi. Singles rate 45000
Coincidences: true 2800
accidental 1600
total 4400

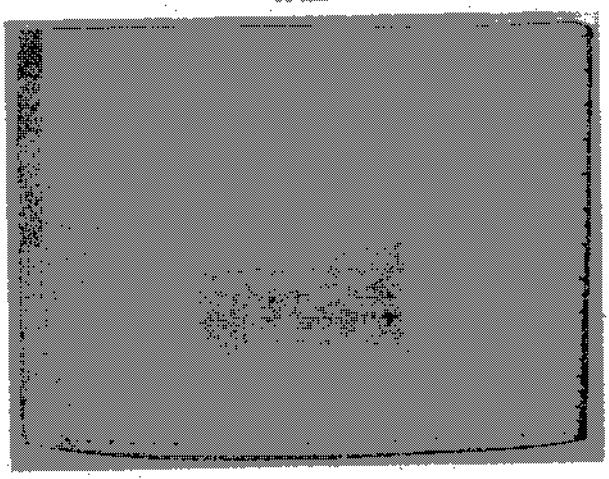

b) 40 μCi. Singles rate 15000
Coincidences: true 1050
accidental 200
total 1250

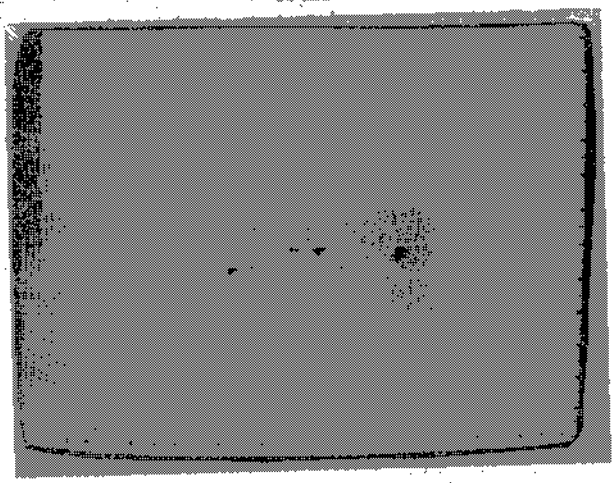

c) 12 μCi. Singles rate 5000
Coincidences: true 330
accidental 20
total 350

Fig. 7: The count rate capability of the camera. The image degrades at the highest rate. $2.5 \cdot 10^5$ events in each image. Bin size 1 × 1 mm.

counting rate to 20,000 c.p.s. From the data of Fig. 7 the present sensitivity is 25 c.p.s. per μCi. Clearly this too will increase by an order of magnitude with the improvement in detection efficiency.

Spatial Resolution

The factors which degrade the image quality include the range of the positrons in the object, the angle between the annihilating gamma rays, the finite resolution of the chambers, and the parallax error due to the converter thickness.

Positron range

Positrons, after emission from the nuclei, will travel variable distances before annihilating. This positron range distribution is difficult to calculate from first principles[18] because of the multiple scattering of each positron by the electrons. Good experimental data exists, however, of the form of the distribution[19] and the residual range[20] for a wide range of materials and positron energy. From these two references, we have for 600 keV positrons in aluminium, atomic number 13, a non-Gaussian distribution of FWHM 0.86 mm and FWTM 1.4 mm. Extrapolating to oxygen, atomic number 8, provides an estimate for water of FWHM 2.4 mm and FWTM 3.2 mm. Clearly, the positron range is a significant source of error, particularly for higher energy positrons.

Annihilation angle

The very object of measurement in the first camera application, the difference of the angle between the two photons from 180° is, for medical imaging, a source of error. An estimate of the effect may be made from angular correlation data for water and ice[21]. The distribution for water at 22°C is non-Gaussian with a FWHM of 8.5 mrads and a FWTM of 17.0 mrads. Projected onto a chamber at a distance of 10 cm, this is equivalent to 0.85 mm, and it therefore contributes 0.43 mm to resolution uncertainty on the camera midplane.

Chamber resolution

The intrinsic spatial resolution of a chamber is 1.2 mm FWHM, see Fig. 3. However, for gamma-rays incident at an angle θ to the chamber there is an additional contribution due to the lack of knowledge of the depth of the photon conversion point in the converter. The conversion probability is approximately exponential with depth, and the width of the spread function is equal to $t \cdot \tan\theta$, for a converter of thickness t. Integration over the detector yields a function that is almost triangular in shape with a FWHM of $t/2 \tan\theta_{max}$, where θ_{max} is the maximum incident angle[13]. This parallax effect has been investigated experimentally by imaging a point source of ^{22}Na. Figure 8 shows how the error builds up rapidly with θ to 5.0 mm at 25°. This is with a converter thickness of 2.6 cm.

Over-all resolution

Since some of the error distributions are highly non-Gaussian, the over-all spatial resolution was obtained by convolution. For a 1 mm point source, the result is a FWHM of 2.7 mm, which was checked experimentally for the point source in air and water: see Fig. 9. Agreement is reasonable: the measured spatial resolution in air is 2.4 ± 0.2 mm. It is interesting to observe the effect of Compton scattering in the 15 cm water bath. The FWHM degrades only slightly to 2.6 mm; the background increases, but remains random.

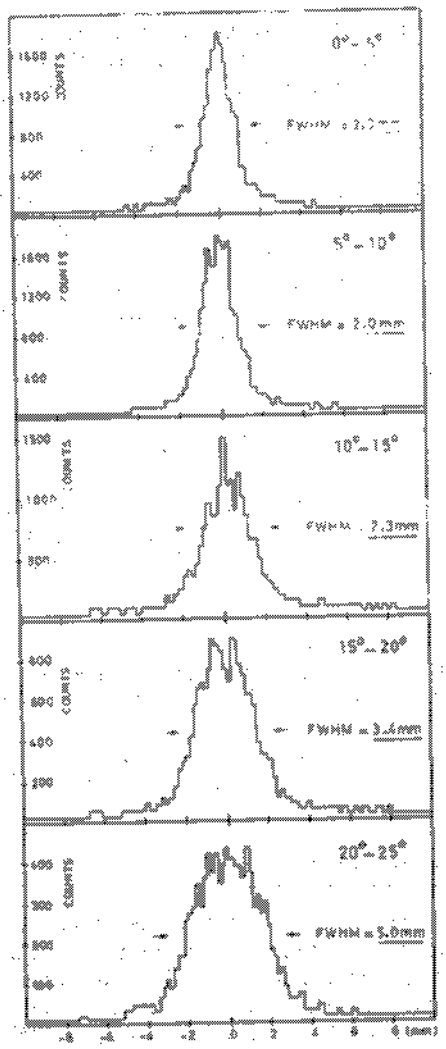

Fig. 8: The converter parallax error as a function of gamma-ray angle. Converter thickness 2.6 cm.

Tomographic Reconstruction

The camera produces focused tomograms of the activity distribution in the object. Each tomogram consists of a single plane in focus, with defocused contributions from all other planes superimposed. Mathematical reconstruction is required to remove the off-plane smearing, and produce a sequence of sharply-focused object activity distributions. Two methods have been used: a pseudo-three-dimensional method in which the blurred background is eliminated from a sequence of two-dimensional planes through the object,[22] and a full three-dimensional approach where the blurring is removed from a three-dimensional lattice containing the measured object activity distribution.[23]

The general imaging process is expressed mathematically as a Fredholm equation,

$$\hat{f}(\underline{\chi}) = \iiint f(\underline{\chi}') \cdot h(\underline{\chi},\underline{\chi}')\, d\underline{\chi}' \quad , \qquad (5)$$

where $\hat{f}(\underline{\chi})$ is the measured (blurred) activity distribution, $f(\underline{\chi}')$ is the true activity distribution, and $h(\underline{\chi},\underline{\chi}')$ is the Green's function of the imaging system. Although in general this response function is not space-invariant, it may become so if sufficient restrictions

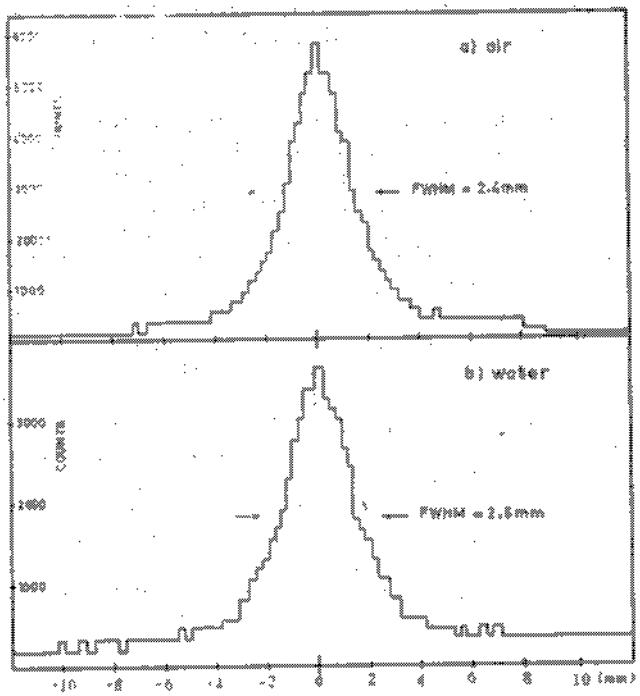

Fig. 9: The experimentally measured camera point-spread function in (a) air and (b) water.

are placed on the emission data, e.g., elimination of wide-angle events to avoid edge effects. Under such a simplifying assumption, Eq. (5) becomes:

$$\hat{f}(\underline{\chi}) = \iiint f(\underline{\chi}') \cdot h(\underline{\chi}-\underline{\chi}')\, d\underline{\chi}' \quad , \qquad (6)$$

which is a three-dimensional convolution integral. In practice, such an integral equation is often solved in Fourier space, where the convolution becomes a product:

$$\hat{F}(\underline{\nu}) = F(\underline{\nu}) \cdot H(\underline{\nu}) \qquad (7)$$

and $\hat{F}(\underline{\nu})$ represents the Fourier transform of $\hat{f}(\underline{\chi})$, etc. Different instabilities in the solution of Eq. (6) arise depending on which of the two reconstruction methods mentioned above are used.

Sequence of planes

The object is reconstructed on a sequence of planes $i = 1 \ldots N_p$, for which the imaging process becomes:

$$\hat{f}_j(x,y) = \sum_i \iint f_i(x',y')\, h_{ij}(x-x',y-y')\,dx'dy' \qquad (8)$$

where the response function $h_{ij}(x-x',y-y')$ is a matrix that gives the response at (x,y) in plane j to a point source at x',y' in plane i. In Fourier space this becomes:

$$\hat{F}_j(\nu_x\nu_y) = \sum_i F_i(\nu_x\nu_y) \cdot H_{ij}(\nu_x\nu_y) \qquad (9)$$

with a formal solution

$$F_i(\nu_x\nu_y) = \sum_j \hat{F}_j(\nu_x\nu_y) \cdot H^{-1}_{ij}(\nu_x\nu_y) \quad . \qquad (10)$$

Unfortunately, the response function for an imaging system such as Fig. 6, becomes very small at low frequencies, with a singularity in $H^{-1}_{ij}(\nu_x\nu_y)$ at $\nu_x = \nu_y = 0$.

The singularity itself is no problem since it means $F_j(v_x v_y)$ may be determined only to within an arbitrary constant, i.e., the absolute activity of each plane is unknown. The behaviour of $H_{ij}^{-1}(v_x v_y)$ close to $v_x \simeq v_y \simeq 0$ is more troublesome since it causes amplification of the statistical fluctuations inherent in $\hat{F}_j(v_x v_y)$.

Rather than leaving the low frequencies in $\hat{F}_j(v_x v_y)$ completely unmodified, $H_{ij}^{-1}(v_x v_y)$ has been determined by a generalized inversion procedure,[6] using a singular value decomposition for the matrix $H_{ij}(v_x v_y)$. The decomposition expresses $H_{ij}^{-1}(v_x v_y)$ as a sum over its eigenvalues and eigenvectors. The sum may be cut at a level consistent with the statistical fluctuations inherent in $\hat{F}_j(v_x v_y)$, thereby preventing the elements of H_{ij}^{-1} becoming too large. The effectiveness of such a procedure is seen in Fig. 10, where the first row shows a set of simulated focused tomograms containing the letters A, B, C and an empty plane, respectively. The result of leaving the low frequencies unmodified during reconstruction is shown in row two, while rows three and four show two different cut-offs in the singular value decomposition for $H_{ij}^{-1}(v_x v_y)$. A significant improvement in background elimination is clearly seen. The cut-off level may be related directly to the average statistical noise in the focused tomogram $\hat{F}_j(v_x v_y)$.

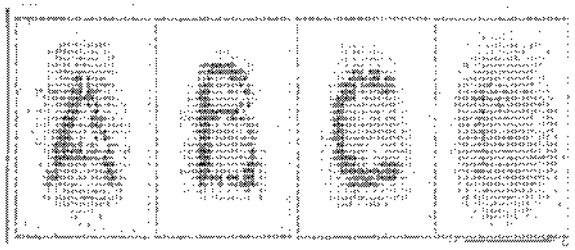

a) original tomograms

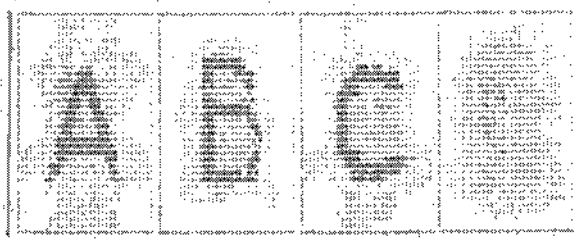

b) no low-frequency correction

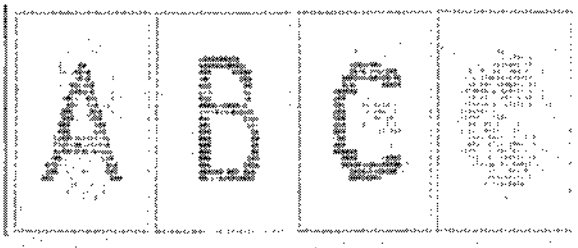

c) $\lambda_c = 0.5$

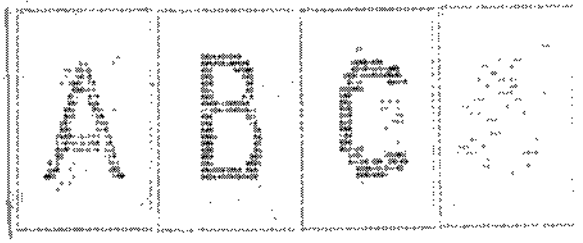

d) $\lambda_c = 0.1$.

Fig. 10: The reconstruction of a simulated extended object on four planes.

The inverse Fourier transform of Eq. (10) then gives the true activity distribution for plane i.

Three-dimensional lattice

Equation (6) may be solved directly in three dimensions leading to Eq. (7). In this equation $H(\underset{\sim}{\chi})$ is a simple scalar and the solution for $F(\underset{\sim}{\chi})$ is:

$$F(\underset{\sim}{\chi}) = \hat{F}(\underset{\sim}{\chi})/H(\underset{\sim}{\chi}) \quad . \tag{11}$$

In this approach, no attempt is made to determine the absolute activity of subsections of the object, and thus the low frequency problems discussed previously do not apply. $H(\underset{\sim}{\chi})$ at $\underset{\sim}{\chi} = 0$ is the over-all normalization of the response function, which is arbitrary. However, in three dimensions high frequency fluctuations become important, and it is found necessary to replace Eq. (11) by:[23]

$$F(\underset{\sim}{\chi}) = \hat{F}(\underset{\sim}{\chi})/\left[H(\underset{\sim}{\chi}) + (2\pi)^4 \cdot \gamma v^4/H(\underset{\sim}{\chi})\right] \tag{12}$$

where γ is a constant whose value depends on the level of statistical fluctuations in $\hat{F}(\underset{\sim}{\chi})$, and which represents a smoothing of the high frequency components of $F(\underset{\sim}{\chi})$.

The sharp cut-off in the transfer function $H(\underset{\sim}{\chi})$, particularly in the direction perpendicular to the detectors, requires the inclusion of a smoothing "window" function in order to reduce spurious high-frequency oscillations in $F(\underset{\sim}{\chi})$. As reported in ref. 23, a Gaussian window is found to be superior to the more usual Hanning function.

Construction of $\hat{f}(\underset{\sim}{\chi})$

The first stage in the reconstruction is to convert the photon position measurements into a function $\hat{f}(\underset{\sim}{\chi})$. Each photon pair defines a line joining the two detectors. In the first method, this line is intersected with each of the j planes, and the bin containing the intersection point is incremented by one. Repeating this for all events produces a set of two-dimensional histograms $\hat{f}_j(x,y)$, $j = 1 \ldots N_p$.

In the second method, $H(\underset{\sim}{\chi})$ is defined in terms of a scalar field of the form:

$$\frac{\cos^n \theta}{r^2/\cos\theta + a^2} \quad , \qquad r^2 = x^2 + y^2 + z^2$$

where a is the bin size in the x,y projection and θ is the angle of the line defined by the photon pair. The arbitrary power n gave best results for $n = -3$. Thus, for each event line intersecting a bin, the contents of the bin is incremented by a weight $\cos^n \theta$, which, when repeated for all events, leads to a three-dimensional scalar field $\hat{f}(\underset{\sim}{\chi})$.

Computing time

The time taken for image reconstruction is dominated, in both methods, by the time to construct $\hat{f}(\underset{\sim}{\chi})$. The maximum speed achieved for such a calculation on an IBM 370/168, using integer arithmetic and table look-up, was 6000 events/sec for lattice dimensions of 128 × 128 × 16. Thus, for 10^6 events, the scalar field calculation takes 170 secs. This is to be compared with a time of 15 sec for a three-dimensional Fourier transform of the same lattice, and 6 sec to perform the operation of Eq. (12). The over-all image reconstruction time for

an activity distribution of dimensions 25 × 25 × 16 cm^3 with a resolution of 2 mm × 2 mm × 10 mm is of the order of 3.5 mins for 10^6 events.

Phantom Imaging

A comparison of the two methods outlined above showed no substantial difference in the reconstructions. The plane method tended to be more stable with respect to edge effects and statistical fluctuations in the focused tomograms, with the correct choice of cut-off in the generalized inverse being important. The three-dimensional scalar field tended to give sharper images, particularly for complex object distributions, but was less stable to statistical fluctuations. The actual choice of γ [Eq. (12)] proved to be extremely important, but often rather difficult, with the image quality dependent on the precise value. The background distribution tended to be smoother for the first method, an important fact if background subtraction is to be attempted.

In general, for imaging the high contrast objects described below, either method may be used with almost identical results.

Cone phantom

A small, hollow lucite box 2cm × 2 cm × 4 cm containing a solid cone with base diameter 2 cm and length 3 cm was filled with a 10 μCi ^{22}Na solution. This phantom was placed between the detectors as shown in Fig. 11a. The focused tomograms before reconstruction are shown in Fig. 12a, with the corresponding reconstructions in Fig. 12b. Four successive planes are displayed, with an interplaner spacing of 1.5 cm, and a resolution element of size 1 mm × 1 mm. The defocused background is clearly evident on the original tomograms and is removed by the reconstruction, particularly in the fourth plane which was outside the phantom. Figure 12c shows the result (after reconstruction) of surrounding the phantom with 10 cm of plastic of density 1.4 g/cc. The increase in the background level is due to Compton scattering of the gamma rays, but this does not appear to degrade the quality of the reconstructed image, providing it is of sufficiently high contrast.

Cone phantom with tubes

The phantom described above was imaged for the orientation shown in Fig.11b, with the addition of 3mm diameter plastic tubes positioned 2 cm away and containing 10% of the activity of the cone phantom. The focused tomograms obtained for this phantom are shown in Fig.13a, where the plane separation is 1 cm. The first plane cuts through the cone, whilst the fourth plane contains only defocused background due to the tubes. Between the outline of the box and the results after reconstruction in Fig. 13b. The shadow of the box in plane 4 has been completely eliminated, leaving the tubes clearly visible, and with a width of 3-4 mm. The background between the tubes at one end is an artifact caused by edge effects, and it is completely eliminated by using bigger planes for reconstruction. Some background remains on the intermediate third plane. In the first plane the cone is seen at one end of the cone phantom and a small air bubble at the opposite end. The difference in the intensities of the box and tubes is also apparent.

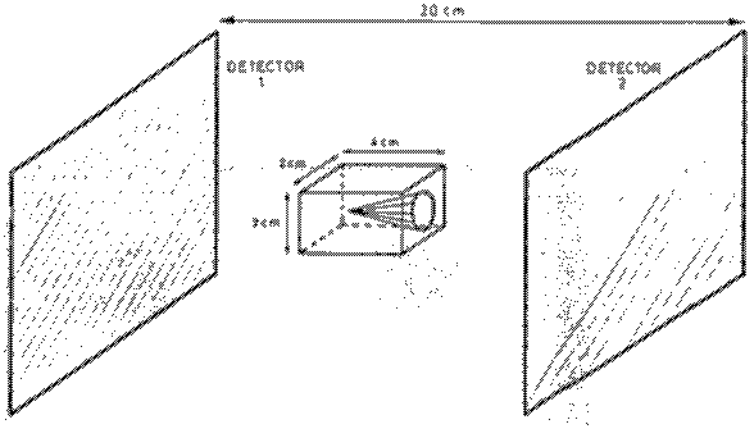

a) cone phantom

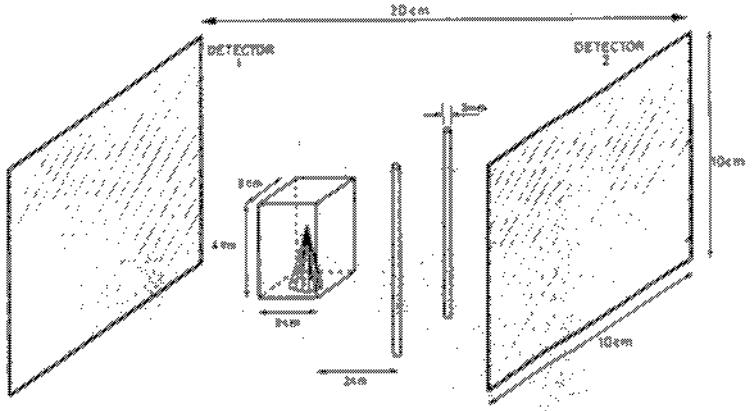

b) cone phantom with lower intensity tubes.

Fig. 11: The schematic layouts for phantom imaging.

This test illustrates well the usefulness of the reconstruction by eliminating the defocused image of the cone phantom from the fourth plane and leaving the much less intense tubes that were genuinely in focus on that plane.

Imaging of a Mouse in Vivo

A solution containing positron-emitting ^{18}F was injected into the tail vein of a mouse. Approximately 0.2 ccs entered the blood stream, corresponding to a total activity of 5.7 μCi, about half of which is taken up by the skeleton[24] within one half to one hour of the injection. The whole body dose is therefore about 0.07 rad, compared with 0.48 rad to the bone. ^{18}F has a half life of 110 mins, decaying by emission of a positron of maximum energy 0.635 MeV.

Half an hour after the ^{18}F injection, the mouse was anaesthetized and, supported in a small plastic cage, placed midway between the two detectors, with its main axis parallel to the plane of the chambers. The position of the mouse within the cage is shown by the X-ray photograph in Fig. 14. Imaging was performed for two hours at a rate of about 100 c.p.s. (limited by the decaying source strength), in order to accumulate $5 \cdot 10^5$ coincidences. The results, after reconstruction, are shown in Fig. 15, where the separation of successive planes is 5 mm and each element corresponds to 1 mm × 1 mm in space.

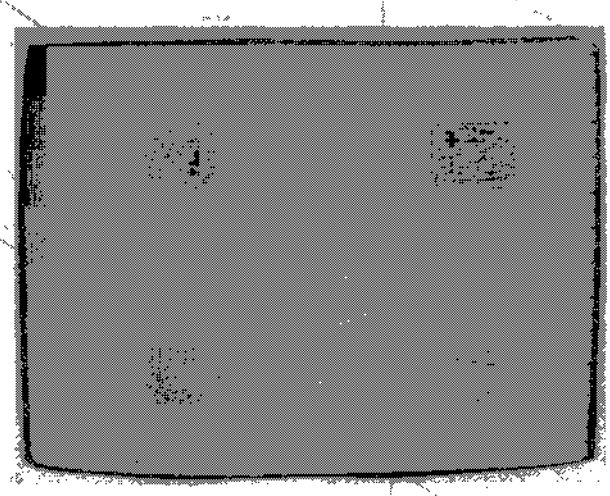

a) tomograms before reconstruction

b) after reconstruction

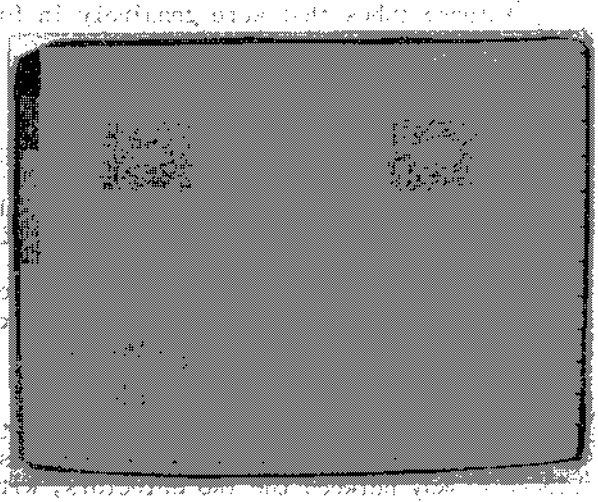

c) with Compton scattering by 10 cm of plastic, after reconstruction.

Fig. 12: Cone phantom imaging on four planes.

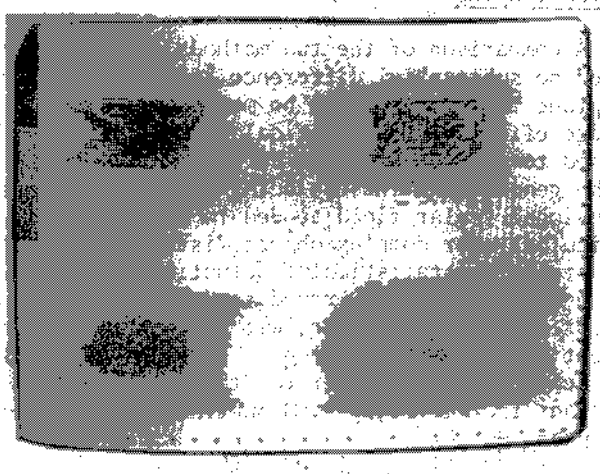

a) tomograms

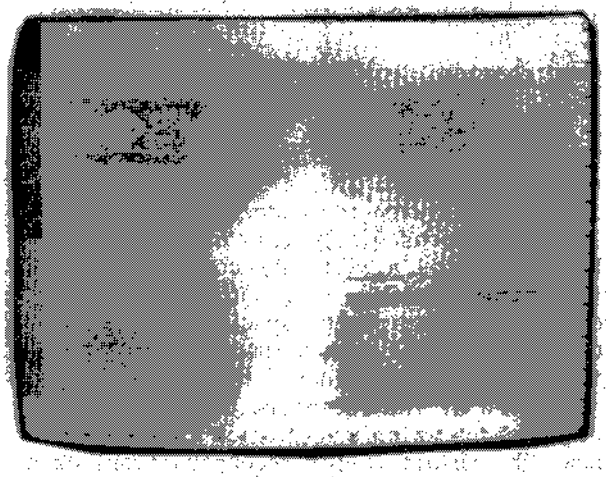

b) reconstructed images.

Fig. 13: Multiple source imaging. Note how the reconstruction completely separates the cone phantom from the much less intense tubes.

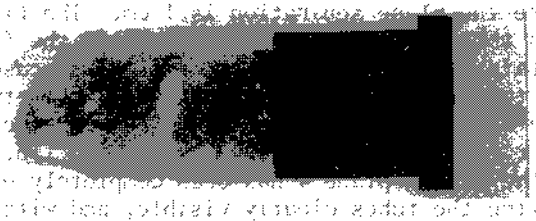

Fig. 14: An X-ray photograph of the mouse secured in its cage.

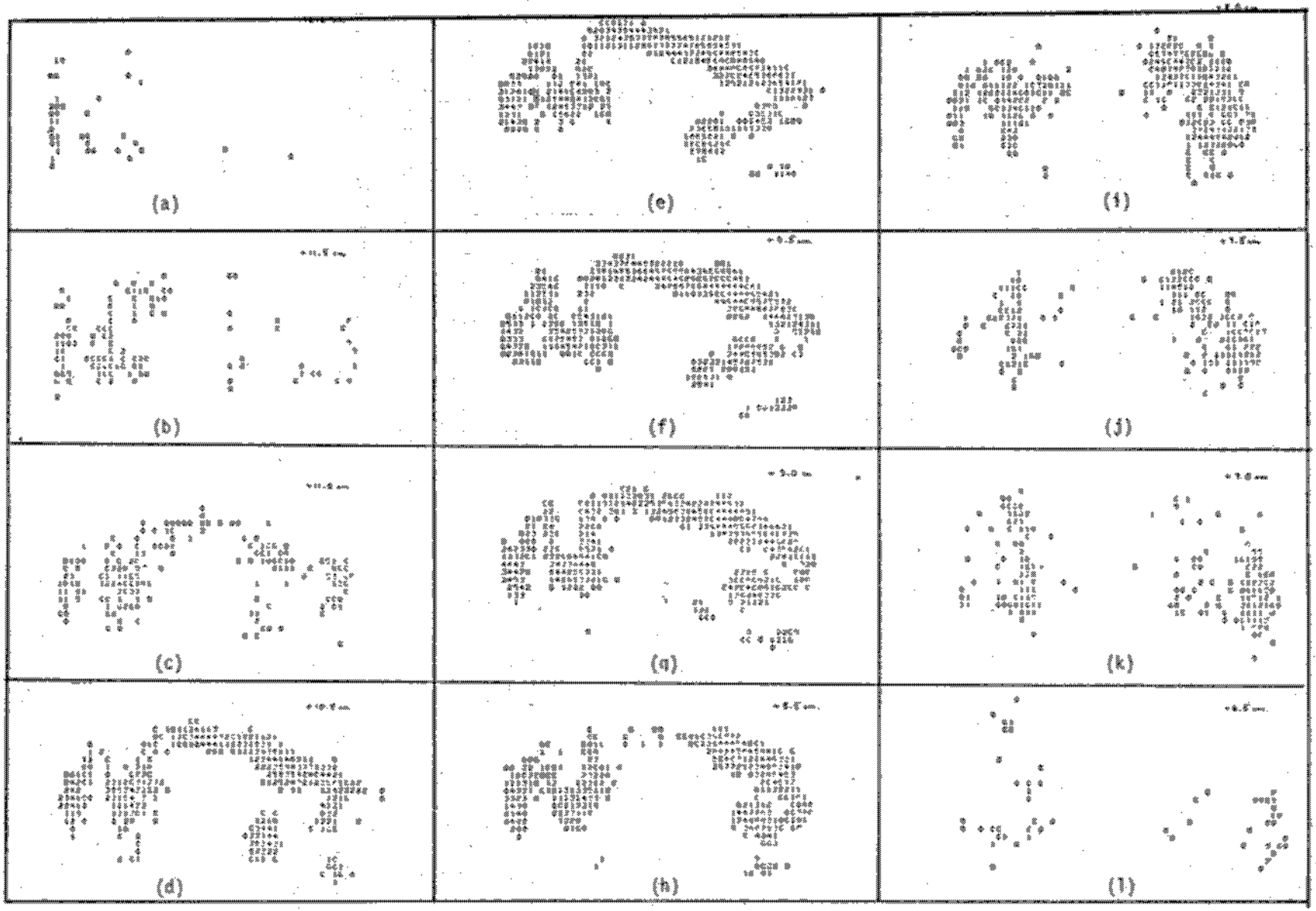

Fig. 15: Reconstructed sections of a mouse following an injection of 5.7 μCi of ^{18}F. Bone structure is clearly revealed. Plane spacing 5 mm. Bin size 1 mm × 1 mm. $4 \cdot 10^5$ events.

The excellent tomography, at the level of 5 mm^3, is obvious as successive planes pass from one side of the mouse to the other. Intermediate planes clearly show the spine, neck and skull, with the two rear legs appearing separately in focus. Indication of a rib cage appears on sections (e) and (f) and again on section (i): the disappearance of the spine in sections (h) and (i) is due to the fact that the mouse was twisted in the supporting cage with its backbone nearer one chamber than the other.

The most striking feature of the image is the appearance in sections (e) to (h) of a very high activity region near the lower end of the spine. This may be due to substantial ^{18}F uptake in the kidneys or bladder, or possibly to activity from the spine and thigh that appear superimposed in this view because of the asymmetry of the mouse. Imaging with the main axis perpendicular to the chambers provided transverse sections, but with only 50,000 coincidences because of the rapidly decaying source strength. These sections, though rather inconclusive, tend to favour the explanation of a superimposition of spine and thigh.

Conclusion

A new type of positron camera with a high spatial resolution has been described and successfully applied to two problems: the measurement of the angular correlation distributions of annihilation radiation, and the direct visualization of radioisotope distributions. A larger camera, 50 × 50 cm, is now planned. Design improvements will provide slightly better spatial resolution of 2 mm FWHM, a much increased data rate of 20,000 c.p.s. and sensitivity of 250 c.p.s. per μCi.

Acknowledgements

We wish to thank Dr. M. Myers and his colleagues at the Hammersmith Hospital, London, for supplying the ^{18}F isotope, and Mlle. M. Bianchi of the Health and Safety Division, CERN, for providing and injecting the mouse. We are also grateful to numerous colleagues and friends in the Data Handling Division, CERN, for discussions and support.

References

1. H.O. Anger, *in* "Instrumentation in Nuclear Medicine", G.J. Hine (Ed.), Vol. 1, pp. 485-552 (Academic Press (1967).
2. A.P. Jeavons, G. Charpak and R.J. Stubbs, Nucl. Instrum. Methods 124, 491 (1975).
3. A.P. Jeavons and C. Cate, IEEE Trans. Nucl. Sci. NS-23, 640 (1976).
4. A.T. Stewart and L.O. Roellig (Eds.), Positron Annihilation (Academic Press) (1967).
5. G.L. Brownell and C.A. Burnham, *in* Instrumentation in Nuclear Medicine, G.J. Hine (Ed.), Vol. 2, pp. 135-159 (Academic Press) (1974).
6. D.W. Townsend, C. Piney and A.P. Jeavons, submitted to Phys. Med. Biol.
7. A.P. Jeavons, N. Ford, B. Lindberg, C. Parkman and Z. Hajduk, IEEE Trans. Nucl. Sci. NS-23, 259 (1976).
8. A.P. Jeavons and A. Manuel, presented at the 4th Int. Conf. on Positron Annihilation, Helsingor, Denmark (1976).
9. Z.H. Cho, M.B. Cohen, M. Singh, L. Eriksson, J. Chan, N. MacDonald and L. Spolter, IEEE Trans. Nucl. Sci. NS-24, 532 (1977).
10. C.A. Burnham and G.L. Brownell, IEEE Trans. Nucl. Sci. NS-19, 201 (1972).
11. E.J. Hoffman, M.E. Phelps, N.A. Mullani, C.S. Higgins and M.M. Ter-Pogossian, J. Nucl. Med. 17, 493 (1976).
12. S.E. Derenzo, T.F. Budinger, J.L. Cahoon, R.H. Huesman and H.G. Jackson, IEEE Trans. Nucl. Sci. NS-24, 544 (1977).
13. G. Muehllehner, M.P. Buchin and J.H. Dudek, IEEE Trans. Nucl. Sci. NS-23, 528 (1976).
14. R.S. Hattner, C.B. Lim, S.J. Swann, L. Kaufman, V. Perez-Mendez, D. Chu, J.P. Huberty, D.C. Price and C.B. Wilson, IEEE Trans. Nucl. Sci. NS-23, 523 (1976).
15. R.A. Reynolds, R.E. Snyder and T.R. Overton, Phys. Med. Biol. 20, 136 (1975).
16. M.J. Neumann, IEEE Trans. Nucl. Sci. NS-24, 515 (1977).
17. E. Bateman, Rutherford Lab., private communication.
18. L.V. Spencer, Phys. Rev. 98, 1597 (1955).
19. H.H. Seliger, Phys. Rev. 100, 1029 (1955).
20. A.T. Nelms, Energy loss and range of electrons and positrons, Nat. Bureau of Standards (Washington), Circ. 577 (1956).
21. P. Colombino, B. Fiscella and L. Trossi, Nuovo Cimento 38, 707 (1965).
22. L.T. Chang, B. Macdonald and V. Perez-Mendez, LBL 3872 (1975).
23. G. Chu and K. Tam, Phys. Med. Biol. 22, 245 (1977).
24. M. Blau, W. Nagler and M.A. Bender, J. Nucl. Med. 3, 332 (1962).